

# Improving Sensitivity of Vector-like Top Partner Searches with Jet Substructure

Anupam Ghosh <sup>1,\*</sup>, Soumyadip Ghosh,<sup>2,†</sup> Soureek  
Mitra <sup>3,‡</sup>, Tousik Samui <sup>4,§</sup> and Ritesh K. Singh <sup>2,¶</sup>

<sup>1</sup>*Department of Physics, Indian Institute of Technology Guwahati,  
North Guwahati, 781039, Assam, India*

<sup>2</sup>*Department of Physical Sciences, Indian Institute of Science  
Education and Research Kolkata, Mohanpur, 741246, Nadia, India*

<sup>3</sup>*Department of Physical Sciences, Indian Institute of Science Education and Research,  
Knowledge City, Sector 81, S. A. S. Nagar, Manauli PO 140306, Punjab, India*

<sup>4</sup>*The Institute of Mathematical Sciences, IV Cross Road,  
CIT Campus, Taramani, Chennai 600113, India*

## Abstract

Vector-like quark partners appear in many BSM models and remain an important area of research, as they can offer insights into the electroweak symmetry breaking mechanism. In this work, we have focused on studying the production of a heavy vector-like top partner in association with a SM top quark via chromomagnetic coupling and the four decay modes of the top partner, namely,  $bW$ ,  $tZ$ ,  $th$ , and  $tg$ . The signal has been studied in final states with one fat jet, at least one  $b$ -tagged jet, one lepton, and missing energy. This study focuses on the extensive use of jet substructure techniques in jets clustered with fixed and dynamically varying radius to deal with events containing differently sized jets. Important kinematic information, along with jet substructure and event shape observables, has been used in a multivariate analysis to extract signal with high significance. A comparative study between fixed and dynamically varying radius clustering of jets is also presented, leading to an improvement in signal sensitivity in the highly boosted scenario.

---

\* [anupamg@rnd.iitg.ac.in](mailto:anupamg@rnd.iitg.ac.in)

† [sg22rs009@iiserkol.ac.in](mailto:sg22rs009@iiserkol.ac.in)

‡ [soureekmitra@iisermohali.ac.in](mailto:soureekmitra@iisermohali.ac.in)

§ [tousiks@imsc.res.in](mailto:tousiks@imsc.res.in)

¶ [ritesh.singh@iiserkol.ac.in](mailto:ritesh.singh@iiserkol.ac.in)

## I. INTRODUCTION

The search for new physics beyond the standard model (BSM) remains one of the most important goals of current and future high-energy collider experiments. Despite many successes, the standard model (SM) of elementary particles leaves several fundamental questions unanswered, such as the nature of electroweak symmetry breaking [1–3], the origin of mass hierarchies [4, 5], matter-antimatter asymmetry [6, 7], the composition of dark matter [8, 9], etc. Many BSM models [10, 11] propose the existence of new resonances, such as vector-like fermions [12–14], that can provide critical insights into some of these open problems and offer experimentally verifiable predictions at the TeV scale [15]. Vector-like fermions are directly related to the stability of the electroweak vacuum [16]. A vector-like top partner, being a color triplet and having the same electric charge as the SM top quark, couples to the Higgs boson and alters the renormalization group evolution of the Higgs quartic coupling. Its Yukawa interaction contributes positively to the running of the Higgs quartic coupling, while mixing with the SM top reduces the top Yukawa contribution that typically drives the coupling negative. Together, these effects slow down or prevent the Higgs quartic coupling from turning negative at high energy scales, thus stabilizing the electroweak vacuum all the way up to the Planck scale. In addition, colored vector-like fermions can mediate interactions between dark matter and SM quarks as indicated in the phenomenological analyses of vector-like portal dark matter models [17–20]. Thus identifying such states would not only signify the discovery of new physics phenomena; but also provide a profound understanding of the structure of fundamental interactions. Extraction of rare BSM signals from overwhelming SM backgrounds requires improved analysis techniques and theoretical modelling. State-of-the-art jet substructure methods [21, 22], clustering algorithms [23], and machine learning techniques [24, 25] have become indispensable tools for identifying boosted heavy resonances and complex event topologies that are characteristic of various BSM signatures at the Large Hadron Collider (LHC). At the same time, access to high-quality data samples, such as CMS Open Data [26, 27], allows for a more reliable background model and realistic performance estimates.

In this work, we investigate the production of a heavy vector-like top partner ( $T$ ) in association with a SM top quark, mediated through chromomagnetic interactions [28, 29]. The top partner decays through four main channels:  $tZ$ ,  $th$ ,  $tg$ , and  $bW$ ; each leading to distinct final state signatures. Among these, direct searches at the LHC have been performed primarily in the  $tZ$  and  $th$  channels, leading to stringent lower limits on the mass of the top partner around a few TeV [30–32]. Furthermore, indirect constraints on the BSM nature of the  $tg$  coupling have been derived using  $t\bar{t}$  events [33, 34]. However, only a handful of direct searches in the  $bW$  decay mode have been performed at the LHC with full Run-II data [35] due to its limited sensitivity. Hence, we put careful focus on the  $bW$  mode of the  $T$  quark decay along with the usual modes in this article.

The nature of modern BSM searches require exploration at increasingly higher energy regimes. At these high energies, fat jets frequently arise from the hadronic decays of boosted heavy particles such as top quarks or heavy bosons, after parton showering and hadronization. One of the primary aspect of this paper is to assess the efficacy of the recently proposed “Dynamic radius” (DR) jet clustering algorithm [36], which is potentially advantageous in the higher energy regime where such fat jets are prominent. The substructure of the fat jets originating from massive boosted particle decays differs significantly from that of narrow QCD jets owing to their decay history,. The DR algorithm leverages this substructure – more precisely, combinations of energy correlation functions [37] to adaptively set the jet radius based on local kinematics, thus producing variable-sized jets in an event. Some recent studies have made use of the DR clustering algorithm with zero pile up sceanrio as indicated in Refs. [38–40]

However, understanding the performance of this algorithm in realistic experimental conditions is extremely crucial. This is the first study incorporating full detector simulation including a realistic model for pile up, to evaluate the robustness of the DR jet clustering method under practical LHC-like conditions.

The final state for this study consists of exactly one lepton, exactly one fat jet, at least one narrow jet that is  $b$ -tagged, and missing transverse momentum ( $p_T^{\text{miss}}$ ), capturing event topologies sensitive to the presence of vector-like top partners. The probe for the signal process is conducted using jets clustered using traditional fixed-radius as well as the more recent dynamic radius approaches. We employ powerful jet substructure tools, namely Soft Drop (SD) grooming [41],  $N$ -subjettiness [42], and energy correlation functions (ECFs) [37] to better understand the nature and the behavior of the fat jet in the event. In addition, we also studied several event shape variables, such as Sphericity [43, 44], Aplanarity [45], Fox-Wolfram moments ( $H$ ) [46, 47] etc., along with lepton and jet kinematic information in a multivariate analysis (MVA), to effectively distinguish signal events from the background. The signal events are simulated with MADGRAPH5\_AMC@NLO [48, 49] together with PYTHIA8 [50] for hadronization and parton showering and DELPHES [51] for detector response modelling. For SM backgrounds, high statistics Monte Carlo (MC) samples from CMS Open Data have been utilized for a reliable estimate. This study also includes pileup simulation with a realistic value of the mean pileup interactions, considering the Run-II LHC conditions.

The article is organized as follows. Section II A introduces the signal model based on chromomagnetic coupling between the vector-like top partner and the SM top quark, while the description of signal and background simulation procedures are presented in Sections II B and II C. The DR algorithm and relevant jet substructure techniques are presented in Section III. Section IV discusses the event reconstruction and selection strategy. In Section V, we detail the multivariate analysis strategy, optimization methods, and present our main results. Finally, Section VI provides a summary of the work and an outlook towards the future prospects.

## II. SIGNAL AND BACKGROUND PROCESSES

### A. Signal model

The vector-like  $T$  quark is a triplet under  $SU(3)$ , and its electric charge is determined by its hypercharge and isospin structure. Additionally, it can couple with any generation of the SM quark. We assume the heavy top partner predominantly interacts with the third-generation SM quarks. The  $T$  quark is a singlet under weak isospin and has the same electromagnetic charge as the top quark; hence, it mixes with the top quark. The general Lagrangian terms are given below [28, 29].

$$\mathcal{L}_{TWb} = -\frac{g_w \sin \theta_L}{\sqrt{2}} \bar{T} \gamma^\mu P_L b W_\mu + h.c., \quad (1)$$

$$\mathcal{L}_{TZt} = \frac{g_w}{2c_w} \bar{t} \gamma^\mu (2 \sin \theta_L \cos \theta_L P_L + \sin \theta_R \cos \theta_R P_R) T Z_\mu + h.c., \quad (2)$$

$$\mathcal{L}_{Th} = -s_w \frac{\sin \theta_R \cos \theta_R}{2M_W} \bar{t} (M_T P_L + m_t P_R) T h + h.c. \quad (3)$$

Here,  $t$  and  $h$  denote the SM top quark and higgs boson, respectively.  $P_{L/R} = \frac{1 \mp \gamma_5}{2}$  represent the left and right-handed projection operators. The mixing angle between the left-handed (right-handed) SM top quark and the left-handed (right-handed)  $T$  quark is denoted by  $\theta_L$

( $\theta_R$ ). The symbols  $M_T$ ,  $m_t$ , and  $M_W$  represent the masses of the  $T$  quark, the SM top quark, and the  $W$  boson, respectively. The  $SU(2)_L$  gauge coupling is  $g_w$ ;  $s_w$  and  $c_w$  are sine and cosine of the electroweak mixing angle. The single production of the exotic  $T$  quark in association with the SM top quark, is possible at the LHC via gluon fusion. The effective Lagrangian of such interactions is as follows.

$$\mathcal{L}_{tg} = \frac{g_s}{\Lambda} G_{\mu\nu}^a [C_{tRL}\bar{T}\sigma^{\mu\nu}\tau^a P_L t + C_{tLR}\bar{T}\sigma^{\mu\nu}\tau^a P_R t] + h.c. \quad (4)$$

where  $\sigma_{\mu\nu} = i/2 (\gamma_\mu\gamma_\nu - \gamma_\nu\gamma_\mu)$ , and  $g_s$  is the SM strong coupling constant. The notation  $G_{\mu\nu}^a$  represents the gluon field strength tensor, and  $\tau^a$  corresponds to the  $SU(3)$  generators.  $C_{tRL}$  and  $C_{tLR}$  are the coupling strengths. We set the new physics scale  $\Lambda = 8$  TeV for our phenomenological analysis. A smaller or larger value of  $\Lambda$  will result in a correspondingly larger or smaller production cross-section, respectively. However, the signal efficiency remains unchanged as long as the mass of the  $T$  quark is fixed.

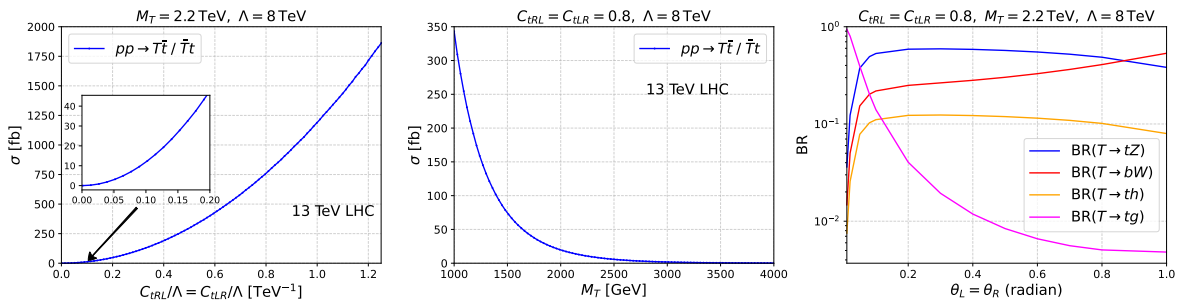


FIG. 1. Variation of cross section with the coupling (left) and with the top-partner ( $T$ ) mass (middle) for the associated production of  $T$  with the SM top quark at the 13 TeV LHC are presented. In these plots, we set the new physics scale  $\Lambda = 8$  TeV. For the left plot,  $M_T$  is set at 2.2 TeV, whereas the couplings  $C_{tRL} = C_{tLR}$  are set to 0.8 for the middle plot. The variation of the branching ratio with the mixing angle is presented for all four decay modes of the top-partner in the right. Here we set  $M_T = 2.2$  TeV,  $C_{tRL} = C_{tLR} = 0.8$ , and  $\Lambda = 8$  TeV.

Fig. 1 shows the variation of the partonic cross section for  $T$ -quark production in association with a top quark at the 13 TeV LHC, along with the branching ratios of its various decay channels, for a fixed new physics scale of  $\Lambda = 8$  TeV. As seen in Eqs.(1)–(3), when the mixing angles are very small ( $\theta_L, \theta_R \rightarrow 0$ ), the branching ratios for  $T \rightarrow tZ$ ,  $T \rightarrow bW$ , and  $T \rightarrow th$  become negligibly small, and the  $T$  quark decays predominantly into a top quark and a gluon. However, with increasing mixing between the  $T$  quark and the top quark, the branching fractions into the electroweak channels  $T \rightarrow tZ$ ,  $T \rightarrow bW$ , and  $T \rightarrow th$  increase significantly.

## B. Signal simulation

The process we are interested in is the production of a SM top quark and its vector-like partner  $T$  via the effective chromomagnetic interaction.

$$pp \rightarrow t\bar{T} + X, \quad \text{and} \quad (5)$$

$$pp \rightarrow T\bar{t} + X. \quad (6)$$

A set of representative parton-level Feynman diagrams corresponding to the process has been given in Fig. 2. For further study and discussion of our result, we chose a benchmark scenario as follows:

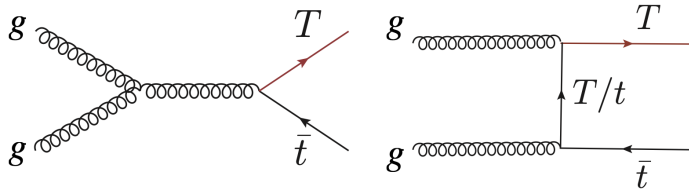


FIG. 2. Representative parton level Feynman diagrams for the process  $pp \rightarrow T\bar{t} + \bar{T}t$ .

$$\frac{C_{tRL}}{\Lambda} = \frac{C_{tLR}}{\Lambda} = 0.1 \text{ TeV}^{-1}, \quad \theta_L = \theta_R = 0.06 \text{ radian}, \quad \text{and } M_T = 2.2 \text{ TeV}. \quad (7)$$

To simulate the processes indicated by Eqs. (5) and (6), we first implemented all the interaction terms defined in Eqs.(1)–(4), along with the SM Lagrangian, using FEYNRULES [52, 53] to generate a Universal FeynRules Output (UFO) [54] model file. This UFO model was then used in the MADGRAPH5\_AMC@NLO framework to generate parton-level events at a centre-of-mass energy of 13 TeV with the parton distribution function (PDF) set to NNPDF30\_nlo\_nf\_5\_pdfas PDFset [55]. The factorization and renormalization scales are set to the default dynamical scale in MADGRAPH5, which corresponds to the transverse mass of the  $2 \rightarrow 2$  scattering process at leading order (LO). The generated events are then passed through PYTHIA8 [50] for parton showering and hadronization. In the PYTHIA8 simulation, the CMS TUNE MONASHSTAR [56], based on Monash 2013 tune [57], has been used to better match CMS data, especially to model the underlying event, initial-state radiation, and beam remnants. Finally, a fast detector simulation is performed using DELPHES [51] to incorporate detector effects. The parton-level kinematics of the produced top partner is shown in Fig. 3 for various mass hypotheses. The higher tail of the  $p_T$ –spectrum of the  $T$  quark has a distinct dependence on its mass. The cross section of the signal process, the  $T$  quark decay width, and its branching fractions for all of the four decay modes are listed in Appendix B for different mass hypotheses.

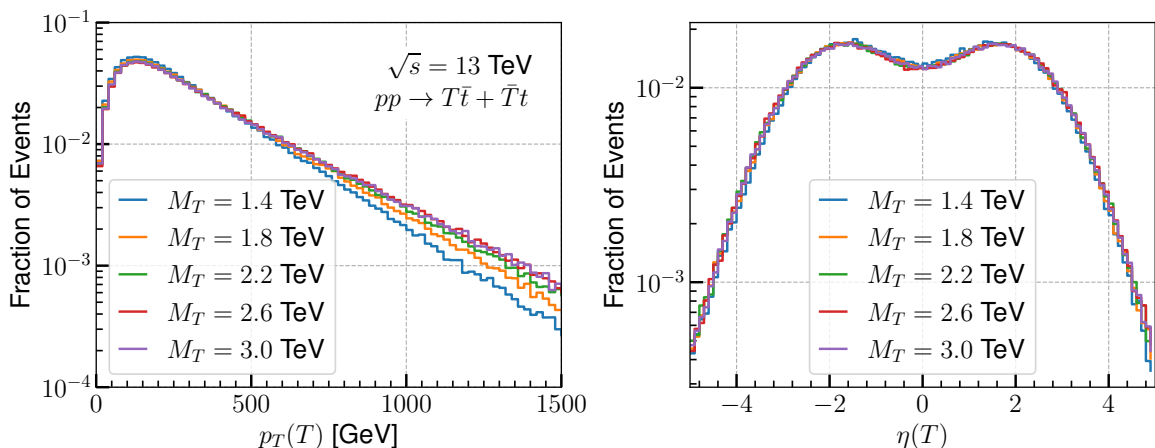


FIG. 3. Parton-level distributions of  $p_T$  (left) and  $\eta$  (right) of the top partner for different mass hypotheses.

Depending on the decay mode of the top partner into  $tZ$ ,  $th$ ,  $tg$ , or  $bW$ , the above processes

could be realized into different event categories. To suppress a huge QCD multijet background at the LHC, we focus on the semi-leptonic channels requiring one lepton ( $\ell = e, \mu$ ) in the final state. Therefore, the final states where one of the  $W$ 's originating from either of the  $t, \bar{t}, T$ , or  $\bar{T}$  decay leptonically, are studied. The event sample for our search can be broadly classified into following two categories:

$$\text{Two fat jets category : } 1\ell + 2 \text{ fat jets} + b\text{-jet} + p_{\text{T}}^{\text{miss}}, \quad (8)$$

$$\text{One fat jet category : } 1\ell + 1 \text{ fat jet} + b\text{-jet(s)} + p_{\text{T}}^{\text{miss}}. \quad (9)$$

Table I lists the different decay modes of the top partner and their possible contribution to each event category. The signal fractions are larger in the two fat jets event category for all decay modes. However, in this event category, the  $t\bar{t} + X$  ( $X = W, Z, \text{jets etc.}$ ) backgrounds also have significantly larger contribution leading to poor signal-to-background ratio and thus making it unsuitable as a search region for the signal process. Therefore, we focus on the one fat jet category where the contribution of the  $bW$  decay mode is relatively higher.

TABLE I. Overall simulated sample sizes ( $N_{\text{Events}}$ ) of the signal process for different decay modes of the  $T$  quark along with their respective contributions to each event category.

	Decay mode			
	$T \rightarrow tZ$	$T \rightarrow th$	$T \rightarrow tg$	$T \rightarrow bW$
$N_{\text{Events}}$ (in Millions)	1.0	1.0	1.0	0.6
Two fat jets category	73.00%	72.03%	76.11%	65.89%
One fat jet category	27.00%	27.97%	23.89%	34.11%

### C. Background processes

Several SM processes that constitute the same final state as that of the signal are considered as backgrounds. The background MC samples are obtained from the CMS Open Data. Table II summarizes these background processes together with their respective cross sections. In the case of  $t\bar{t} + \text{jets}$  background, MC samples binned in  $H_{\text{T}}$  are stitched with the so-called inclusive sample according to the method described in Ref. [58] for better statistical modelling of the boosted topology. Table III summarizes the stitching weights applied to events lying in different  $H_{\text{T}}$  bins. For the QCD multijet background, a combination of different MC samples in non-overlapping  $\hat{p}_{\text{T}}$  bins above 15 GeV is considered.

## III. JET ALGORITHM AND SUBSTRUCTURE METHODS

### A. Dynamic radius jet clustering algorithm

The jet clustering algorithms are crucial steps in the analysis of events in a hadron collider experiment such as the LHC [23, 72]. The currently used algorithms are fixed-radius sequential recombination inclusive jet algorithms, namely the  $k_{\text{T}}$  (KT), anti- $k_{\text{T}}$  (AK), and Cambridge – Aachen (CA) [73–75] algorithms. These traditional algorithms take a list of four-momenta of the particles produced in an event by the process of recombining one or more of these particles into several jets. In their iterative steps, these algorithms calculate pair-wise “ $k_{\text{T}}$ ” distance ( $d_{ij}$ )

TABLE II. List of SM backgrounds along with their respective cross sections and MC sample sizes.

Process	Cross section [pb]	Accuracy	$N_{\text{Events}}$ (in Millions)
$t\bar{t}$ + jets [59]	833.900 [60]	NNLO + NNLL	117.70
$t(\bar{t})W$ + jets [61]	79.300 [62]	NNLO	2.00
$t\bar{t}Z$ [63]	0.863 [64]	NLO + NNLL	22.16
$t\bar{t}W$ [65]	0.745 [66]	NNLO (QCD) + NLO (EW)	0.83
WZ + jets [67]	56.850 [68]	NNLO	13.19
WW + jets [69]	1.371 [70]	NNLO	8.92
QCD multijet [71]	$1.981 \times 10^9$	LO	97.19

TABLE III. Stitching weights for  $t\bar{t}$  + jets events in different  $H_T$  bins for  $300 \text{ fb}^{-1}$  integrated luminosity.

	$H_T$ bins [GeV]				
	[0, 600)	[600, 800)	[800, 1200)	[1200, 2500)	$\geq 2500$
Stitching weights	2.562	$2.550 \times 10^{-2}$	$1.413 \times 10^{-2}$	$9.180 \times 10^{-3}$	$2.154 \times 10^{-4}$

between  $i^{\text{th}}$  and  $j^{\text{th}}$  particles and  $i^{\text{th}}$  particle “beam” distance ( $d_{iB}$ ), defined as

$$d_{ij} = \min(p_{T,i}^{2n}, p_{T,j}^{2n}) \Delta R_{ij}^2, \text{ and} \quad (10)$$

$$d_{iB} = p_{T,i}^{2n} R^2 \quad (11)$$

to decide whether to merge two four-momenta or declare a particular four-momentum as a final jet. Here,  $\Delta R_{ij}$  is the distance between  $i^{\text{th}}$  and  $j^{\text{th}}$  particles in the pseudorapidity-azimuth ( $\eta$ - $\phi$ ) plane. The two four-momenta are merged to give a new four-momentum if  $d_{ij}$  becomes the least among all the pair-wise “ $k_T$ ” and beam distances. Otherwise, the  $i^{\text{th}}$  four-momentum corresponding to the least beam distance is declared as a final jet. Importantly, the algorithm has parameters  $n$ , which usually takes values  $-1$ ,  $0$ , and  $1$  corresponding to AK, CA, and KT algorithms, and  $R$  as the radius parameter. These fixed-radius jet algorithms output jets with a fixed cone size, which is provided through the input parameter  $R$  to the algorithm. Thus, they have the limitation of producing varying-sized jets in an event for a given  $R$  parameter. Several interesting attempts have been made to modify the algorithm to accommodate jets of variable sizes; such as “Variable  $R$ ” jets [76], “Fuzzy” jets [77], “SHAPER” [78], “XCone” [79], “PAIReD” jets [80], “dynamic radius” jets [36] etc.

In this study, we use the “Dynamic radius” jet clustering algorithm [36], which attempts to dynamically modify the jet radius during the evolution of each jet through the iterative steps of the algorithm. The approach is to start from an initial radius  $R_0$ , the radius for each evolving “proto-jet” gets modified depending on its internal structure during the process of clustering. The square of the additive modifier  $\sigma_i$  that is added to each evolving proto-jet at each interactive

stage is given by

$$\sigma_i^2 = \frac{\sum_{a<b} p_T^a p_T^b \Delta R_{ab}^2}{\sum_{a<b} p_T^a p_T^b} - \left( \frac{\sum_{a<b} p_T^a p_T^b \Delta R_{ab}}{\sum_{a<b} p_T^a p_T^b} \right)^2, \quad (12)$$

where  $a$  and  $b$  run over the constituents of the pseudojet. So, the final radius for the  $i^{\text{th}}$  jet becomes  $R_{\text{fin}} = R_0 + \sigma_i$ . The advantage one gets in this method is that the radius is no longer fixed; it gets adapted to the requirement of the jet that is being formed. The modifier is a slight variation of a combination of a few jet substructure observable ECFs [37], which tends to become larger for top or heavy boson jets [81]. On the other hand, it tends to be smaller for narrow jets like the ones appearing from light quarks or gluons. Since our study involves one fat jet along with narrow  $b$ -jets, the efficiency of the dynamic radius jet clustering is expected to be better.

## B. Jet substructure and parameter choices

Improving signal sensitivity over the backgrounds using jets and their substructures is the primary aim of this work. We present here a brief overview of the various jet substructure methods that are used in our analysis.

- **Soft Drop Grooming:** To mitigate contamination from pileup, underlying events, etc., inside a jet, and improve the reliability of the jet substructure measurements, we have used the Soft Drop de-clustering method [41]. This method primarily aims to remove soft and wide-angle radiations inside a jet while retaining the hard core of the jet. To briefly describe, the Soft Drop algorithm is applied on a jet that has been re-clustered using a sequential clustering algorithm such as CA, KT, or AK. The essential step of this method is to remove soft and wide-angle subjet after de-clustering the jet into two subjets (labelled as  $i$  and  $j$ ) by checking the following condition.

$$\frac{\min(p_{T,i}, p_{T,j})}{p_{T,i} + p_{T,j}} < z_{\text{cut}}^{\text{SD}} \left( \frac{\Delta R_{ij}}{R^{\text{SD}}} \right)^{\beta^{\text{SD}}} \quad (13)$$

Here,  $p_{T,i}$  and  $p_{T,j}$  are the transverse momenta of the subjets,  $\Delta R_{ij}$  is the distance between them in the  $\eta$ - $\phi$  plane. This process is repeated until the condition fails to be satisfied. The radius  $R^{\text{SD}}$  is the characteristic jet radius usually taken to be the radius parameter used during the clustering. In case of the dynamic radius jet clustering algorithm, we have taken this parameter to be  $R_d = R_0 + \sigma$ , the final dynamically adjusted radius for each jet.

The two parameters of Soft Drop are (1)  $z_{\text{cut}}^{\text{SD}}$ : energy fraction threshold and (2)  $\beta^{\text{SD}}$ : angular exponent regulating the angular separation between the two subjets. In the special case of  $\beta = 0$ , the method reduces to the Modified Mass-Drop Tagger [82, 83]. The grooming then depends only on the momentum fraction  $z$  and not on the angular separation. We have used the value of  $\beta^{\text{SD}} = 0.0$  to keep our analysis aligned with the available jet substructure measurement [81]. We also check the alternative value of 1.0. For the energy fraction threshold parameter, a nominal value of  $z_{\text{cut}}^{\text{SD}} = 0.1$  is used to match the studies performed in Refs. [41, 84–86].

- **$N$ -subjettiness:** The jet substructure method  $N$ -subjettiness [42], provides a measure

of the consistency of jet having  $N$  subjets inside. In our event topology, we expect boosted top fat jet, which gives rise to a three-prong structure corresponding to its decay products:  $t \rightarrow bW \rightarrow bq\bar{q}$ . Therefore, this method becomes particularly useful with the value of  $N = 3$ . The  $N$ -subjettiness observable captures these subjets by fitting  $N$  subjet axes inside the fat jet. This is performed by minimizing the  $N$ -subjettiness measure [87] defined as

$$\tilde{\tau}_N^{(\beta^{\text{NS}})} = \frac{1}{d_0} \sum_{i \in \text{jet}} p_{T_i} \min \left\{ \Delta R_{i,a_1}^{\beta^{\text{NS}}}, \Delta R_{i,a_2}^{\beta^{\text{NS}}}, \dots, \Delta R_{i,a_N}^{\beta^{\text{NS}}} \right\}, \quad (14)$$

where the sum runs over all constituents in the jet, and  $\Delta R_{i,a_k}$  is the distance in  $\eta$ - $\phi$  plane between constituent  $i$  and subjet axis  $a_k$ . The prefactor  $1/d_0$  is a normalisation factor. The exponent  $\beta^{\text{NS}}$  and the method used to determine the seed  $N$  axes (e.g., exclusive  $k_T$  axes from an iterative algorithm) are parameters of choice. We have used  $N$ -subjettiness method implemented in FASTJET CONTRIB [88]. In our study, we use the ratios  $\tau_{32} = \tau_3/\tau_2$  and  $\tau_{21} = \tau_2/\tau_1$  as a top tagger with  $\beta^{\text{NS}} = 1.0$  and the seed axes obtained via WTA\_KT\_AXES method [89–91].

- **Energy Correlation Functions:** These are a class of infrared and collinear safe observables proposed to study jet properties [37]. The first three lowest point functions take the form

$$\text{ECF}_1(\beta^{\text{ECF}}) = \sum_{i \in J} p_{T_i}, \quad (15)$$

$$\text{ECF}_2(\beta^{\text{ECF}}) = \sum_{i < j \in J} p_{T_i} p_{T_j} \Delta R_{ij}^{\beta^{\text{ECF}}}, \quad (16)$$

$$\text{ECF}_3(\beta^{\text{ECF}}) = \sum_{i < j < k \in J} p_{T_i} p_{T_j} p_{T_k} (\Delta R_{ij} \Delta R_{ik} \Delta R_{jk})^{\beta^{\text{ECF}}}, \quad (17)$$

where the sum is over the jet constituents and the exponent  $\beta^{\text{ECF}}$  is a parameter that gives the weight to the angular separation between the jet constituents. These functions help distinguish between jets originating from different partonic configurations. In case of top quark study, a better discrimination from QCD jets is obtained for  $\beta^{\text{ECF}} = 1.0$  [37]. We therefore choose to use  $\beta^{\text{ECF}} = 1.0$  as a nominal value and  $\beta^{\text{ECF}} = 0.5$  for an alternate value.

Instead of using the ECFs as defined in Eqs.(15) – (17) directly, their ratios are better suited as they remove the  $p_T$  dependence. The following ratios [81] are studied.

$$e_2 = \frac{\text{ECF}_2}{(\text{ECF}_1)^2}, \quad e_3 = \frac{\text{ECF}_3}{(\text{ECF}_1)^3}, \quad (18)$$

$$C_2 = \frac{e_3}{(e_2)^2}, \quad \text{and} \quad D_2 = \frac{e_3}{(e_2)^3}. \quad (19)$$

The dynamic radius jet algorithm, along with the jet substructure methods, has been implemented within DELPHES and CMS SOFTWARE VERSION 7.6.7 as appropriate plugins. The choices of parameters for the jet substructure methods described above for the dynamic radius jets, including both nominal and alternate values used for variations, are summarized in Table IV. The impact of these choices is studied by comparing the shapes of different observables sensitive to the respective substructure methods, as shown in Fig. 4. As seen in the figure, the distributions for nominal and alternate parameter choices look quite similar, suggesting that the overall analysis remains fairly robust against these variations. In addition, the nominal

choice for the dynamic radius jet algorithm is also compared with the fixed-radius counterpart, as shown in Fig. 5.

TABLE IV. Choice of various parameters for dynamic radius fat jets.

Method	Parameter	Nominal Value	Alternate Value
Soft Drop [41]	$\beta^{\text{SD}}$	<b>0.0</b> [81]	1.0
	$z_{\text{cut}}^{\text{SD}}$	<b>0.1</b> [81]	–
$N$ -subjettiness [42]	$\beta^{\text{NS}}$	<b>1.0</b> [81]	–
	Seed Axes [79]	WTA_KT_AXES [84]	–
ECF [37]	$\beta^{\text{ECF}}$	<b>1.0</b> [81]	0.5

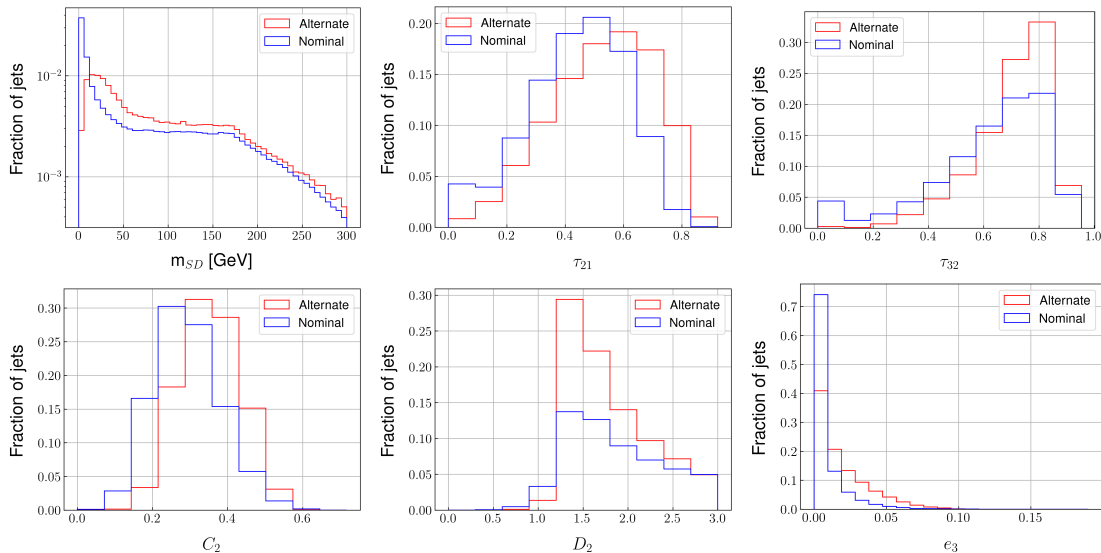


FIG. 4. Comparison of Soft Drop mass (upper-left),  $\tau_{21}$  (upper-middle),  $\tau_{32}$  (upper-right), and the ECF ratios  $C_2$  (lower-left),  $D_2$  (lower-middle), and  $e_3$  (lower-right) distributions of the leading fat jet corresponding to nominal and alternate values of substructure parameters for dynamic radius jets in  $t\bar{t}$  + jets events.

#### IV. EVENT RECONSTRUCTION AND SELECTION

Events having a minimum of one reconstructed pp interaction vertex are retained for this study. The vertices must be reconstructed from at least four tracks that have a longitudinal distance  $|d_z| < 24$  cm and a radial distance  $|d_{xy}| < 2$  cm from the nominal interaction point. If multiple vertices are found in an event, the one with the highest value of summed  $p_T^2$  of clustered particles is taken as the primary pp interaction vertex. In contrast, the others are identified as the pileup vertices. Individual particles are reconstructed via the particle-flow algorithm [92]. Muons (Electrons) are required to have  $p_T \geq 30$  (35) GeV,  $|\eta| \leq 2.4$  (2.1) and to pass the “tight” identification criteria [93, 94]. The selected muon and electron candidates must pass the criterion on relative isolation ( $I_{\text{rel}}$ ) to be within 6% of their respective transverse momentum. Additionally, the selected electron candidate is required to satisfy  $|d_{xy}| \leq 0.05$  (0.1) cm and

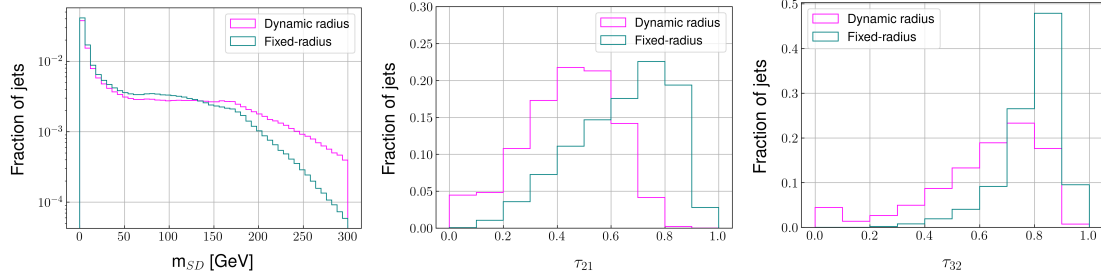


FIG. 5. Comparison of Soft Drop mass (left),  $\tau_{21}$  (middle), and  $\tau_{32}$  (right) distributions of the leading fat jet between fixed- and dynamic radius algorithms in  $t\bar{t} + \text{jets}$  events.

$|d_z| \leq 0.1$  (0.2) cm relative to the primary vertex in the barrel (endcap) region of the electromagnetic calorimeter (ECAL). Events containing additional muons (electrons) with  $p_T \geq 10$  (15) GeV,  $|\eta| \leq 2.4$  (2.5), and passing the “loose” (“veto”) identification criteria are rejected. In such cases, the criteria on the additional lepton isolation are relaxed to  $I_{\text{rel}} \leq 20\%$  for muons and  $I_{\text{rel}} \leq 18\%$  (16%) for electrons in the barrel (endcap) ECAL region. Correction factors for lepton reconstruction efficiencies are applied to simulated events for both selected and vetoed leptons in bins of lepton  $p_T$  and  $\eta$ ; to mitigate observed differences with collision data [93, 94]. Standard jets are reconstructed using the AK clustering algorithm [74] with radii of 0.4 and 0.8 for the narrow (AK4) and fat (AK8) jets respectively, as implemented in the FASTJET package [88]. The effect of additional tracks and energy deposits in calorimeters from pileup on the AK4 and AK8 jet momenta are mitigated by discarding tracks identified to be originating from pileup vertices, as well as by applying an offset correction to account for residual neutral pileup contributions [95, 96]. “Tight lepton veto” identification criteria [97] are applied to suppress jets arising from spurious sources, such as electronic noise in the calorimeters and jets containing “tight”-ly identified muons or electrons. The combined secondary vertex tagging algorithm version 2 (CSVv2) [98] is used to identify AK4 jets originating from bottom quarks or antiquarks. Candidate events are required to have **exactly one** AK8 jet with  $p_T \geq 200$  GeV and within  $|\eta| \leq 4.0$ , as mentioned in Section II B. In addition to the selected AK8 jet, events must have **at least one** non-overlapping AK4 jet with  $p_T \geq 30$  GeV,  $|\eta| \leq 2.5$  and passing the “medium” working point defined on the CSVv2 score. Finally, events should pass  $p_T^{\text{miss}} \geq 30$  GeV criterion.

In addition to the AK4 and AK8 jets, we reconstruct the anti- $k_T$  DR jets (see Section III A) for the selected events<sup>1</sup> using the particle-flow candidate information as input. The DR algorithm is used to form two jet collections per event, corresponding to  $R_0$  values of 0.3 and 0.7 for narrow and fat jets, respectively. The narrow jets that do not overlap with any fat jet in the event, are considered as independent. The CSVv2 score of the nearest AK4 jet is assigned as the b-tagging discriminant value for each narrow jet.

Table V lists signal and background yields after all event selection steps for the two event categories. Figures 6 and 7 show several kinematic distributions after applying all selection criteria in  $e + \text{jets}$  and  $\mu + \text{jets}$  final states, respectively.

<sup>1</sup> The jet selection criteria are applied to AK4 and AK8 jets, and **not to** dynamic radius jets. This choice is made primarily due to the absence of optimized pileup contamination removal, jet identification working points, jet energy resolution and correction etc. for the dynamic radius jets.

TABLE V. Event yields of signal and background processes for the two lepton flavours after applying all selection criteria for an integrated luminosity of  $300 \text{ fb}^{-1}$ .

Final state	Bkg. processes						Total Bkg.	Signal
	$t\bar{t} + \text{jets}$	$t(\bar{t})W + \text{jets}$	$t\bar{t}Z$	$t\bar{t}W$	WV + jets (V = W or Z)	QCD multijet		
$e + \text{jets}$	18313	29544	620	825	4077	35634	89013	25
$\mu + \text{jets}$	69083	99413	2112	3035	13243	63309	250196	15

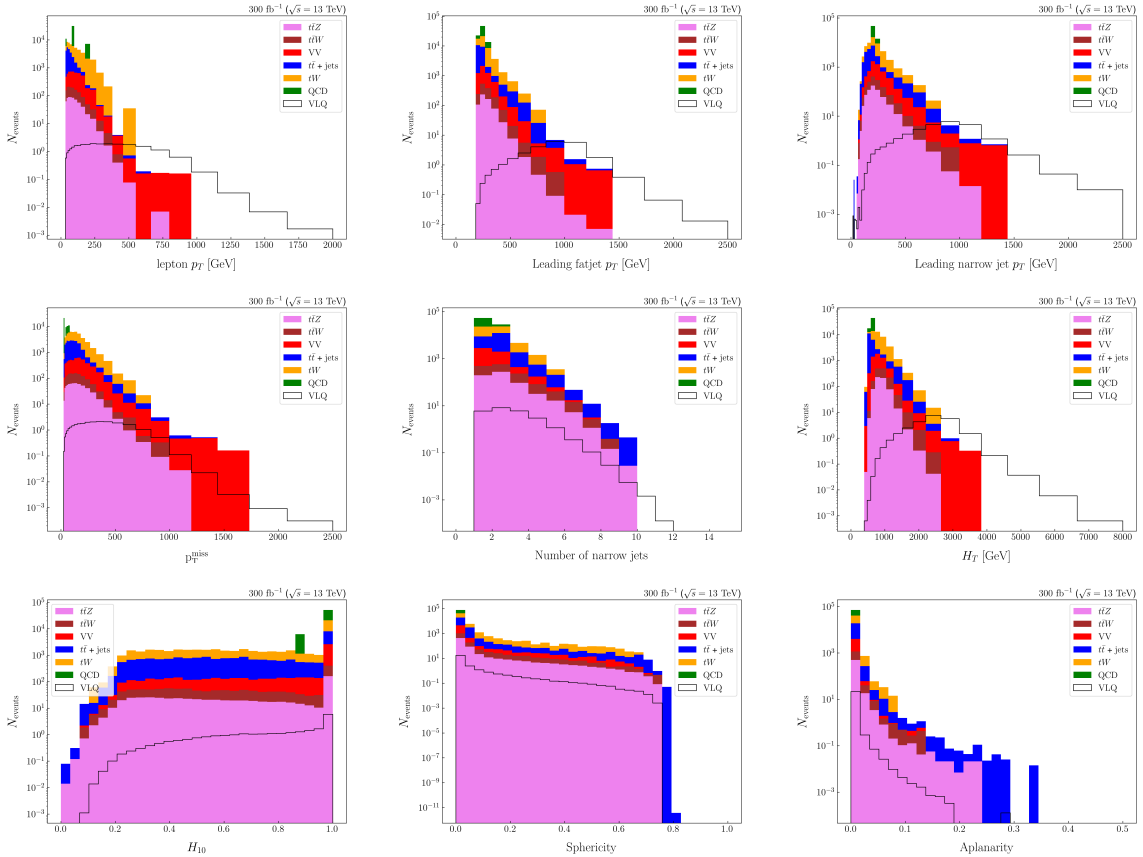


FIG. 6. Distributions of various kinematic and event shape observables in the  $e + \text{jets}$  final state.

## V. RESULTS

Several observables are combined into a boosted decision tree (BDT) discriminant per event category to separate signal from the collective SM backgrounds. These are listed in Appendix A along with the respective ranks based on their importance. The simulated events are separated into two independent sub-samples, one for training and the other for validation, in 70% : 30% ratio. An event is picked randomly to belong to any one of these sub-samples. Each process is weighted according to its purity during training. Two independent trainings are performed, one for fixed-radius jets and another for DR jets. The adaptive boosting algorithm [99] implemented within the TMVA package [100] has been used. A check for overtraining is performed by comparing the respective BDT scores of signal and background between training and validation sub-samples. The corresponding Kolmogorov-Smirnov probabilities range between 32% – 97%, indicating no overtraining. The performance of the BDTs is studied via the receiver-operator

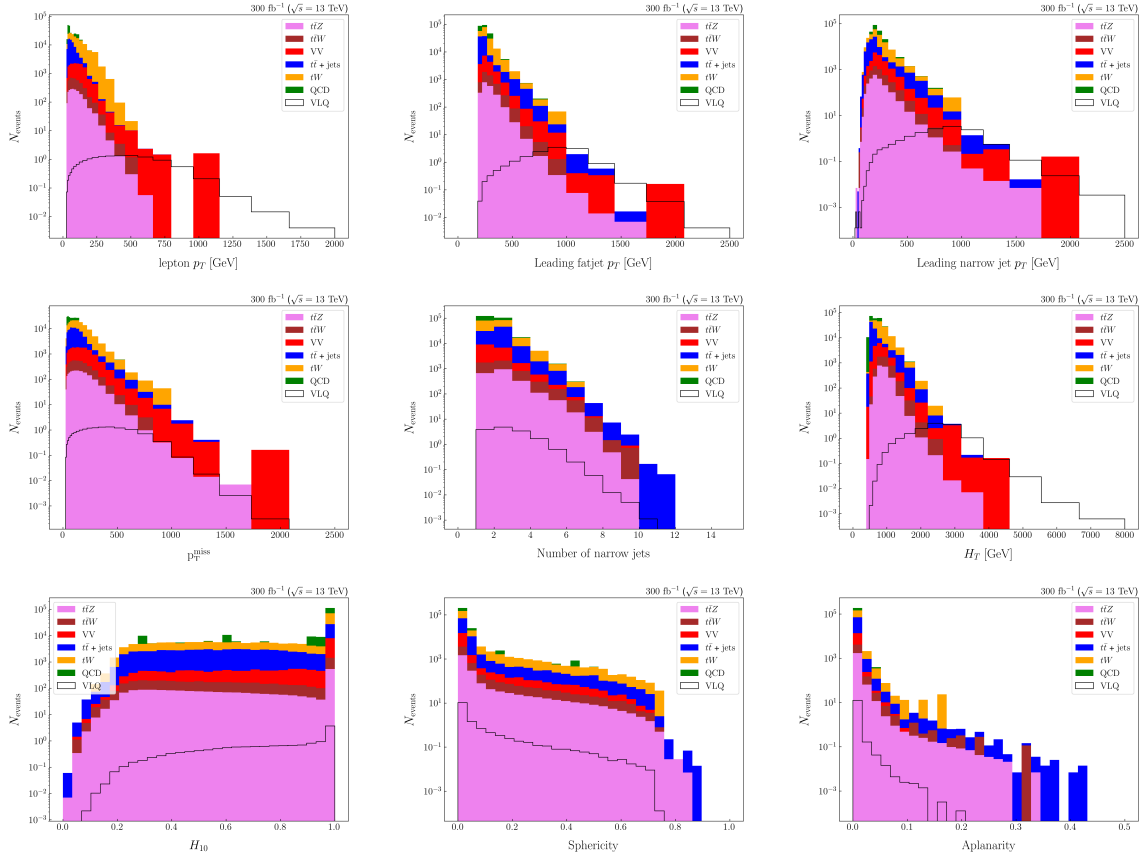


FIG. 7. Distributions of various kinematic and event shape observables in the  $\mu + \text{jets}$  final state.

characteristic (ROC) curves for different thresholds applied to the fat jet  $p_T$ . Figure 8 shows the BDT scores of signal and background as well as comparisons of ROC curves for different fat jet  $p_T$  thresholds for fixed-radius and DR jet algorithms. The BDT performance falls off relatively slower for tighter thresholds on fat jet  $p_T$  in the case of DR jet algorithm as indicated by the ROC curves.

Selection thresholds on the BDT scores are optimized based on the so-called ‘‘Punzi figure-of-merit’’ ( $\text{FOM}_{\text{Punzi}}$ ) defined in Ref. [101]. The variation of the signal significance defined as  $\frac{S}{\sqrt{S+B}}$  and the  $\text{FOM}_{\text{Punzi}}$  are studied with fat jet  $p_T$  threshold for the fixed-radius and DR jet algorithms after applying a selection on the BDT scores  $\geq 0.3$ . From Fig. 9, it is evident that the DR jet algorithm outperforms the fixed-radius one in the **highly boosted** (fat jet  $p_T \geq 750$  GeV) region of the phase space. The adaptive approach adopted by the DR algorithm (see Section III A) ensures that all daughters of the  $T$  quark are essentially captured within the fat jet by optimizing the jet size, which in turn leads to improved reconstruction of the signal events, in this region. The DR algorithm shows higher sensitivity towards large  $M_T$  values (see Fig. 3) compared to the fixed-radius algorithm, allowing for more phase space to hunt for the signal process.

We then calculate expected  $2\sigma$  upper limits on the chromomagnetic couplings, assuming  $C_{tRL} = C_{tLR}$ , for the top partner masses in the range 1.4 TeV to 3 TeV. For each mass point, the upper limit has been obtained by varying the coupling strength such that the signal significance reaches  $2\sigma$ . Figure 10 shows the resulting upper limits for the three different fat jet  $p_T$  thresholds. In the plots, the shaded regions correspond to values of the coupling excluded by our analysis at 95% CL under the assumption of no signal observation. The upper limits are

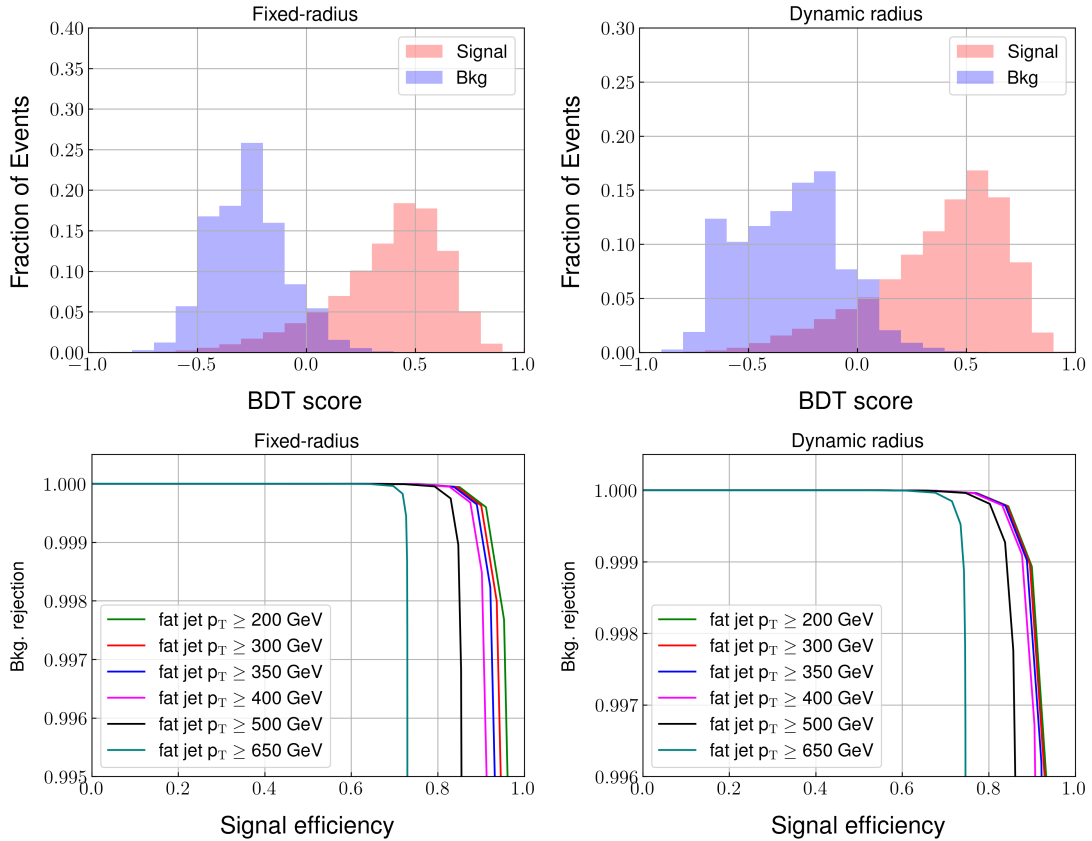


FIG. 8. BDT scores (upper row) along with the ROCs (lower row) for fixed-radius (left) and dynamic radius (right) jets.

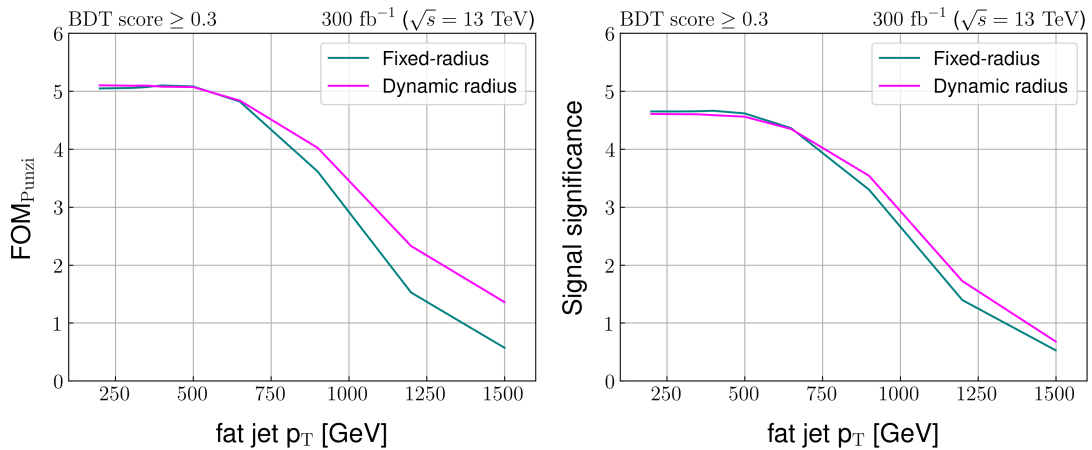


FIG. 9. Comparison of  $FOM_{P_{unzi}}$  (left) and signal significance (right) between fixed-radius and dynamic radius jets with the fat jet  $p_T$  threshold.

estimated using both fixed-radius and DR jet algorithms. In all cases, the expected limit from the DR algorithm is smaller than that from the fixed radius one, indicating that the analysis with dynamic radius jets has better sensitivity to smaller coupling values. The improvement is more prominent for the fat jet  $p_T$  threshold of 900 GeV, suggesting that the dynamic radius jet algorithm is especially effective in the high fat jet  $p_T$  regime.

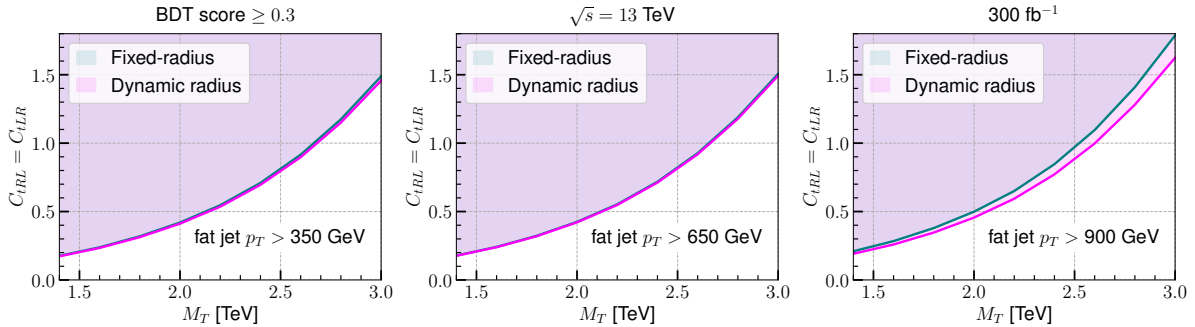


FIG. 10. Expected  $2\sigma$  upper limit on the chromomagnetic coupling  $C_{tRL} = C_{tLR}$  as a function of the top partner mass. The three panels correspond to three different fat jet  $p_T$  thresholds. For these plots, we use  $\Lambda = 8$  TeV, and all other parameters are kept the same as in the benchmark point defined in Eq. (7). Shaded regions indicate the parameter space excluded by our analysis, assuming no signal is observed.

## VI. SUMMARY AND OUTLOOK

In this work, we performed a thorough investigation of collider prospects of a vectorlike top partner produced in association with a standard model top quark via a chromomagnetic coupling. The top partner is assumed to decay into the following channels:  $tZ$ ,  $th$ ,  $tg$ , or  $bW$ . To effectively suppress the huge QCD background, we focused on semileptonic final states, i.e., events with exactly one isolated lepton arising either from the top quark or from the heavy boson decay. Depending on the decay modes of the top partner, the final state could contain one or two fat jets along with a single lepton and  $b$ -tagged jet(s). We performed the analysis in the event category that contains single fat jet ( $1\ell + 1$  fat jet +  $\geq 1$   $b$ -tagged jet) due to its comparatively better signal-to-background ratio.

We carried out a detailed collider analysis at the 13 TeV LHC with an integrated luminosity of  $300 \text{ fb}^{-1}$ , incorporating realistic pileup conditions. For signal events, the MADGRAPH5\_AMC@NLO + PYTHIA8 + DELPHES simulation chain has been employed; while for background estimation, appropriate simulated samples from CMS Open Data are utilized. To enhance signal discrimination, we utilized state-of-the-art jet substructure tools such as Soft Drop grooming,  $N$ -subjettiness, and Energy Correlation Functions, along with several event shape observables like Fox-Wolfram moments, Sphericity, and Aplanarity. Multivariate discriminants based on boosted decision trees are developed for better signal-to-background separation. We then optimized a selection thresholds on these discriminants based on the Punzi figure-of-merit to improve signal sensitivity.

The result is presented as the upper limit on the chromomagnetic coupling between the top quark and its heavy vectorlike partner. Assuming the cut off scale of  $\Lambda = 8$  TeV, the upper limit on the coupling is found to lie within 0.2 to 1.5 for the top partner mass range of 1.4 to 3 TeV.

An important aspect of our work is a comparative performance analysis between conventional fixed-radius vs modern dynamic radius clustering of anti- $k_T$  jets under realistic pileup conditions. We observe that the dynamic radius approach enhances the signal sensitivity, particularly in regions with high jet transverse momentum allowing for tighter bounds on the chromomagnetic coupling. This suggests that the dynamic radius jet clustering is more effective in probing high-energy regimes compared to the conventional fixed-radius method.

There remains various scopes for further improvements. Optimization of pile up contamination removal working points as well as determining dedicated jet energy correction and resolution for the dynamic radius clustering approach can be extremely useful. This might put even tighter bounds on the couplings than the existing ones. Future directions also include exploring the use of neural network-based discriminants or adopting a hybrid strategy that combines fixed and dynamic radius clustering depending on the fat jet’s transverse momentum. Such ideas can potentially enhance the reach and robustness of the future studies.

## VII. ACKNOWLEDGMENTS

The authors sincerely acknowledge the organizers of the WHEPP XVII, 2023 for providing a platform to meet and initiate this work. The authors acknowledge the organizers, instructors, and facilitators of the CMS Open Data Workshop at WHEPP XVII, 2023, for the necessary training to access and process CMS Open Data samples. The authors are thankful to the computing facility at IISER Kolkata for the computational and data storage resources.

## DATA AVAILABILITY STATEMENT

This study is based on a combination of simulated data generated using standard HEP packages and simulated data from CMS Open Data repository. The details of the simulation process that support our findings are provided within the article.

- 
- [1] G. F. Giudice, *PoS EPS-HEP2013*, 163 (2013), [arXiv:1307.7879 \[hep-ph\]](#).
  - [2] S. Alekhin, A. Djouadi, and S. Moch, *Phys. Lett. B* **716**, 214 (2012), [arXiv:1207.0980 \[hep-ph\]](#).
  - [3] G. Degrandi, S. Di Vita, J. Elias-Miro, J. R. Espinosa, G. F. Giudice, G. Isidori, and A. Strumia, *JHEP* **08**, 098 (2012), [arXiv:1205.6497 \[hep-ph\]](#).
  - [4] C. D. Froggatt and H. B. Nielsen, *Nucl. Phys. B* **147**, 277 (1979).
  - [5] H. Fritzsch and Z.-z. Xing, *Prog. Part. Nucl. Phys.* **45**, 1 (2000), [arXiv:hep-ph/9912358](#).
  - [6] A. Riotto and M. Trodden, *Ann. Rev. Nucl. Part. Sci.* **49**, 35 (1999), [arXiv:hep-ph/9901362](#).
  - [7] M. Dine and A. Kusenko, *Rev. Mod. Phys.* **76**, 1 (2003), [arXiv:hep-ph/0303065](#).
  - [8] D. Clowe, M. Bradac, A. H. Gonzalez, M. Markevitch, S. W. Randall, C. Jones, and D. Zaritsky, *Astrophys. J. Lett.* **648**, L109 (2006), [arXiv:astro-ph/0608407](#).
  - [9] Y. Sofue and V. Rubin, *Ann. Rev. Astron. Astrophys.* **39**, 137 (2001), [arXiv:astro-ph/0010594](#).
  - [10] M. Perelstein, M. E. Peskin, and A. Pierce, *Phys. Rev. D* **69**, 075002 (2004), [arXiv:hep-ph/0310039](#).
  - [11] O. Matsedonskyi, G. Panico, and A. Wulzer, *JHEP* **01**, 164 (2013), [arXiv:1204.6333 \[hep-ph\]](#).
  - [12] J. A. Aguilar-Saavedra, R. Benbrik, S. Heinemeyer, and M. Pérez-Victoria, *Phys. Rev. D* **88**, 094010 (2013), [arXiv:1306.0572 \[hep-ph\]](#).
  - [13] A. Falkowski, D. M. Straub, and A. Vicente, *JHEP* **05**, 092 (2014), [arXiv:1312.5329 \[hep-ph\]](#).
  - [14] F. del Aguila, L. Ametller, G. L. Kane, and J. Vidal, *Nucl. Phys. B* **334**, 1 (1990).
  - [15] A. Hayrapetyan *et al.* (CMS), *Phys. Rept.* **1115**, 570 (2025), [arXiv:2405.17605 \[hep-ex\]](#).
  - [16] G. Hiller, T. Höhne, D. F. Litim, and T. Steudtner, *Phys. Rev. D* **106**, 115004 (2022), [arXiv:2207.07737 \[hep-ph\]](#).
  - [17] S. Colucci, B. Fuks, F. Giacchino, L. Lopez Honorez, M. H. G. Tytgat, and J. Vandecasteele, *Phys. Rev. D* **98**, 035002 (2018), [arXiv:1804.05068 \[hep-ph\]](#).
  - [18] A. Ghosh and P. Konar, *JHEP* **09**, 104 (2024), [arXiv:2407.01415 \[hep-ph\]](#).
  - [19] A. Ghosh, P. Konar, and R. Roshan, *JHEP* **12**, 167 (2022), [arXiv:2207.00487 \[hep-ph\]](#).
  - [20] A. Ghosh and P. Konar, *Phys. Dark Univ.* **47**, 101746 (2025), [arXiv:2305.08662 \[hep-ph\]](#).

- [21] S. Marzani, G. Soyez, and M. Spannowsky, *Looking inside jets: an introduction to jet substructure and boosted-object phenomenology*, Vol. 958 (Springer, 2019) arXiv:1901.10342 [hep-ph].
- [22] R. Kogler *et al.*, *Rev. Mod. Phys.* **91**, 045003 (2019), arXiv:1803.06991 [hep-ex].
- [23] G. P. Salam, *Eur. Phys. J. C* **67**, 637 (2010), arXiv:0906.1833 [hep-ph].
- [24] J. M. Duarte, *PoS ICHEP2024*, 012 (2025), arXiv:2409.20413 [hep-ex].
- [25] A. Radovic, M. Williams, D. Rousseau, M. Kagan, D. Bonacorsi, A. Himmel, A. Aurisano, K. Terao, and T. Wongjirad, *Nature* **560**, 41 (2018).  
10.7483/OPENDATA.CMS.
- [27] *CERN Open Data Policy for the LHC Experiments*, Tech. Rep. (CERN, Geneva, 2020).
- [28] M. Buchkremer, G. Cacciapaglia, A. Deandrea, and L. Panizzi, *Nucl. Phys. B* **876**, 376 (2013), arXiv:1305.4172 [hep-ph].
- [29] D. Choudhury, K. Deka, and N. Kumar, *Phys. Rev. D* **104**, 035004 (2021), arXiv:2103.10655 [hep-ph].
- [30] G. Aad *et al.* (ATLAS), *JHEP* **05**, 263 (2024), arXiv:2402.16561 [hep-ex].
- [31] A. Tumasyan *et al.* (CMS), *JHEP* **09**, 057 (2023), arXiv:2302.12802 [hep-ex].
- [32] A. Hayrapetyan *et al.* (CMS), *Phys. Rev. D* **110**, 072012 (2024), arXiv:2405.05071 [hep-ex].
- [33] A. Hayreter and G. Valencia, *Phys. Rev. D* **93**, 014020 (2016), arXiv:1511.01464 [hep-ph].
- [34] A. Tumasyan *et al.* (CMS), *JHEP* **06**, 081 (2023), arXiv:2205.02314 [hep-ex].
- [35] A. Tumasyan *et al.* (CMS), *JHEP* **07**, 020 (2023), arXiv:2209.07327 [hep-ex].
- [36] B. Mukhopadhyaya, T. Samui, and R. K. Singh, *JHEP* **04**, 019 (2023), arXiv:2301.13074 [hep-ph].
- [37] A. J. Larkoski, G. P. Salam, and J. Thaler, *JHEP* **06**, 108 (2013), arXiv:1305.0007 [hep-ph].
- [38] D. Kar, W. Nzuza, and S. Sinha, *SciPost Phys. Core* **7**, 071 (2024), arXiv:2207.01885 [hep-ph].
- [39] B. Mukhopadhyaya, S. Samanta, T. Samui, and R. K. Singh, *Phys. Rev. D* **108**, 075004 (2023), arXiv:2305.16403 [hep-ph].
- [40] A. Ghosh, P. Konar, T. Samui, and R. K. Singh, (2025), arXiv:2505.16328 [hep-ph].
- [41] A. J. Larkoski, S. Marzani, G. Soyez, and J. Thaler, *JHEP* **05**, 146 (2014), arXiv:1402.2657 [hep-ph].
- [42] J. Thaler and K. Van Tilburg, *JHEP* **03**, 015 (2011), arXiv:1011.2268 [hep-ph].
- [43] J. D. Bjorken and S. J. Brodsky, *Phys. Rev. D* **1**, 1416 (1970).
- [44] J. F. Donoghue, F. E. Low, and S.-Y. Pi, *Phys. Rev. D* **20**, 2759 (1979).
- [45] G. Aad *et al.* (ATLAS), *Eur. Phys. J. C* **72**, 2211 (2012), arXiv:1206.2135 [hep-ex].
- [46] G. C. Fox and S. Wolfram, *Nucl. Phys. B* **149**, 413 (1979), [Erratum: Nucl.Phys.B 157, 543 (1979)].
- [47] C. Bernaciak, M. S. A. Buschmann, A. Butter, and T. Plehn, *Phys. Rev. D* **87**, 073014 (2013), arXiv:1212.4436 [hep-ph].
- [48] J. Alwall, R. Frederix, S. Frixione, V. Hirschi, F. Maltoni, O. Mattelaer, H. S. Shao, T. Stelzer, P. Torrielli, and M. Zaro, *JHEP* **07**, 079 (2014), arXiv:1405.0301 [hep-ph].
- [49] R. Frederix, S. Frixione, V. Hirschi, D. Pagani, H. S. Shao, and M. Zaro, *JHEP* **07**, 185 (2018), [Erratum: JHEP 11, 085 (2021)], arXiv:1804.10017 [hep-ph].
- [50] C. Bierlich *et al.*, *SciPost Phys. Codeb.* **2022**, 8 (2022), arXiv:2203.11601 [hep-ph].
- [51] J. de Favereau, C. Delaere, P. Demin, A. Giammanco, V. Lemaitre, A. Mertens, and M. Selvaggi (DELPHES 3), *JHEP* **02**, 057 (2014), arXiv:1307.6346 [hep-ex].
- [52] N. D. Christensen and C. Duhr, *Comput. Phys. Commun.* **180**, 1614 (2009), arXiv:0806.4194 [hep-ph].
- [53] A. Alloul, N. D. Christensen, C. Degrande, C. Duhr, and B. Fuks, *Comput. Phys. Commun.* **185**, 2250 (2014), arXiv:1310.1921 [hep-ph].
- [54] C. Degrande, C. Duhr, B. Fuks, D. Grellscheid, O. Mattelaer, and T. Reiter, *Comput. Phys. Commun.* **183**, 1201 (2012), arXiv:1108.2040 [hep-ph].
- [55] R. D. Ball *et al.* (NNPDF), *JHEP* **04**, 040 (2015), arXiv:1410.8849 [hep-ph].
- [56] V. Khachatryan *et al.* (CMS), *Eur. Phys. J. C* **76**, 155 (2016), arXiv:1512.00815 [hep-ex].
- [57] P. Skands, S. Carrazza, and J. Rojo, *Eur. Phys. J. C* **74**, 3024 (2014), arXiv:1404.5630 [hep-ph].
- [58] K. Ehatäht and C. Veelken, *Eur. Phys. J. C* **82**, 484 (2022), arXiv:2106.04360 [physics.data-an].
- [59] “Simulated dataset TTJets TuneCUETP8M1 13TeV-madgraphMLM-pythia8 in MINIAODSIM format for 2015 collision data,” (2021), CERN Open Data Portal, doi:10.7483/OPENDATA.CMS.4UC1.XE6W, doi:10.7483/OPENDATA.CMS.TRGR.ISWK, doi:10.7483/OPENDATA.CMS.QSCL.T5V6, doi:10.7483/OPENDATA.CMS.P6DS.TA9G, doi:10.7483/OPENDATA.CMS.3OFU.QCHW, doi:10.7483/OPENDATA.CMS.ZLCL.5OLD, doi:10.7483/OPENDATA.CMS.NIW3.SWVK, doi:10.7483/OPENDATA.CMS.MY34.FGWJ, doi:10.7483/OPENDATA.CMS.EAFA.TRYV, doi:10.7483/OPENDATA.CMS.T3IH.3GLZ.

- [60] M. Czakon and A. Mitov, *Comput. Phys. Commun.* **185**, 2930 (2014), arXiv:1112.5675 [hep-ph].
- [61] “Simulated dataset tW top and antitop inclusiveDecays 13TeV-powheg-pythia8 TuneCUETP8M1 in MINIAODSIM format for 2015 collision data,” (2021), CERN Open Data Portal, doi:10.7483/OPENDATA.CMS.EKZ2.EXSU, doi:10.7483/OPENDATA.CMS.JG3K.U1HH.
- [62] N. Kidonakis and N. Yamanaka, *JHEP* **05**, 278 (2021), arXiv:2102.11300 [hep-ph].
- [63] “Simulated dataset ttZJets 13TeV madgraphMLM in MINIAODSIM format for 2015 collision data,” (2021), CERN Open Data Portal, doi:10.7483/OPENDATA.CMS.68LT.V5HE.
- [64] A. Kulesza, L. Motyka, D. Schwartzländer, T. Stebel, and V. Theeuwes, *Eur. Phys. J. C* **79**, 249 (2019), arXiv:1812.08622 [hep-ph].
- [65] “Simulated dataset TTWJets TuneCUETP8M1 13TeV-amcatnloFXFX-madspin-pythia8 in MINIAODSIM format for 2015 collision data,” (2021), CERN Open Data Portal, doi:10.7483/OPENDATA.CMS.Y9YE.GSCH, doi:10.7483/OPENDATA.CMS.2J3N.SAEU.
- [66] L. Buonocore, S. Devoto, M. Grazzini, S. Kallweit, J. Mazzitelli, L. Rottoli, and C. Savoini, *Phys. Rev. Lett.* **131**, 231901 (2023), arXiv:2306.16311 [hep-ph].
- [67] “Simulated dataset WZJets 13TeV-pythia8 in MINIAODSIM format for 2015 collision data,” (2021), CERN Open Data Portal, doi:10.7483/OPENDATA.CMS.OT9K.8B6X, doi:10.7483/OPENDATA.CMS.RBRF.G35V, doi:10.7483/OPENDATA.CMS.B0AH.8063, doi:10.7483/OPENDATA.CMS.2IZ1.BFHY.
- [68] M. Grazzini, S. Kallweit, D. Rathlev, and M. Wiesemann, *Phys. Lett. B* **761**, 179 (2016), arXiv:1604.08576 [hep-ph].
- [69] “Simulated dataset WWJets 13TeV-powheg in MINIAODSIM format for 2015 collision data,” (2021), CERN Open Data Portal, doi:10.7483/OPENDATA.CMS.8SBL.SMML, doi:10.7483/OPENDATA.CMS.N1NR.ZKCS.
- [70] M. Grazzini, S. Kallweit, S. Pozzorini, D. Rathlev, and M. Wiesemann, *JHEP* **08**, 140 (2016), arXiv:1605.02716 [hep-ph].
- [71] “Simulated dataset QCD TuneCUETP8M1 13TeV pythia8 in MINIAODSIM format for 2015 collision data,” (2021), CERN Open Data Portal, doi:10.7483/OPENDATA.CMS.9S1H.GPAZ, doi:10.7483/OPENDATA.CMS.AQYT.7JKJ, doi:10.7483/OPENDATA.CMS.XXOE.WFX4, doi:10.7483/OPENDATA.CMS.2ZYM.S9ZX, doi:10.7483/OPENDATA.CMS.WFJA.FPGG, doi:10.7483/OPENDATA.CMS.9OJV.RZ4U, doi:10.7483/OPENDATA.CMS.O3DT.38EH, doi:10.7483/OPENDATA.CMS.5DBS.XCW8, doi:10.7483/OPENDATA.CMS.3Y72.BWW4, doi:10.7483/OPENDATA.CMS.SGRV.4ABD, doi:10.7483/OPENDATA.CMS.WOP0.TFY9, doi:10.7483/OPENDATA.CMS.N49K.1FTR, doi:10.7483/OPENDATA.CMS.KN7J.TCST, doi:10.7483/OPENDATA.CMS.OV3H.MOWO, doi:10.7483/OPENDATA.CMS.RMU2.D9II.
- [72] G. F. Sterman and S. Weinberg, *Phys. Rev. Lett.* **39**, 1436 (1977).
- [73] S. D. Ellis and D. E. Soper, *Phys. Rev. D* **48**, 3160 (1993), arXiv:hep-ph/9305266.
- [74] M. Cacciari, G. P. Salam, and G. Soyez, *JHEP* **04**, 063 (2008), arXiv:0802.1189 [hep-ph].
- [75] M. Wobisch and T. Wengler, in *Workshop on Monte Carlo Generators for HERA Physics (Plenary Starting Meeting)* (1998) arXiv:hep-ph/9907280.
- [76] D. Krohn, J. Thaler, and L.-T. Wang, *JHEP* **06**, 059 (2009), arXiv:0903.0392 [hep-ph].
- [77] L. Mackey, B. Nachman, A. Schwartzman, and C. Stansbury, *JHEP* **06**, 010 (2016), arXiv:1509.02216 [hep-ph].
- [78] D. Ba, A. S. Dogra, R. Gambhir, A. Tasissa, and J. Thaler, *JHEP* **06**, 195 (2023), arXiv:2302.12266 [hep-ph].
- [79] I. W. Stewart, F. J. Tackmann, J. Thaler, C. K. Vermilion, and T. F. Wilkason, *JHEP* **11**, 072 (2015), arXiv:1508.01516 [hep-ph].
- [80] S. Mondal, G. Barone, and A. Schmidt, *JHEP* **09**, 128 (2024), arXiv:2311.11011 [hep-ex].
- [81] M. Aaboud *et al.* (ATLAS), *JHEP* **08**, 033 (2019), arXiv:1903.02942 [hep-ex].
- [82] J. M. Butterworth, A. R. Davison, M. Rubin, and G. P. Salam, *Phys. Rev. Lett.* **100**, 242001 (2008), arXiv:0802.2470 [hep-ph].
- [83] M. Dasgupta, A. Fregoso, S. Marzani, and G. P. Salam, *JHEP* **09**, 029 (2013), arXiv:1307.0007 [hep-ph].
- [84] A. J. Larkoski and J. Thaler, *Phys. Rev. D* **90**, 034010 (2014), arXiv:1406.7011 [hep-ph].
- [85] A. J. Larkoski, S. Marzani, and J. Thaler, *Phys. Rev. D* **91**, 111501 (2015), arXiv:1502.01719 [hep-ph].
- [86] A. M. Sirunyan *et al.* (CMS), *Phys. Rev. Lett.* **120**, 142302 (2018), arXiv:1708.09429 [nucl-ex].
- [87] J. Thaler and K. Van Tilburg, *JHEP* **02**, 093 (2012), arXiv:1108.2701 [hep-ph].
- [88] M. Cacciari, G. P. Salam, and G. Soyez, *Eur. Phys. J. C* **72**, 1896 (2012), arXiv:1111.6097 [hep-ph].

- [89] D. Bertolini, T. Chan, and J. Thaler, *JHEP* **04**, 013 (2014), [arXiv:1310.7584 \[hep-ph\]](#).  
[90] A. J. Larkoski, D. Neill, and J. Thaler, *JHEP* **04**, 017 (2014), [arXiv:1401.2158 \[hep-ph\]](#).  
[91] G. P. Salam, “ $E_t^\infty$  Scheme,” Unpublished.  
[92] A. M. Sirunyan *et al.* (CMS), *JINST* **12**, P10003 (2017), [arXiv:1706.04965 \[physics.ins-det\]](#).  
[93] A. M. Sirunyan *et al.* (CMS), *JINST* **13**, P06015 (2018), [arXiv:1804.04528 \[physics.ins-det\]](#).  
[94] A. M. Sirunyan *et al.* (CMS), *JINST* **16**, P05014 (2021), [arXiv:2012.06888 \[hep-ex\]](#).  
[95] M. Cacciari and G. P. Salam, *Phys. Lett. B* **659**, 119 (2008), [arXiv:0707.1378 \[hep-ph\]](#).  
[96] A. M. Sirunyan *et al.* (CMS), *JINST* **15**, P09018 (2020), [arXiv:2003.00503 \[hep-ex\]](#).  
[97] *Jet algorithms performance in 13 TeV data*, CMS Physics Analysis Summary CMS-PAS-JME-16-003 (2017).  
[98] A. M. Sirunyan *et al.* (CMS), *JINST* **13**, P05011 (2018), [arXiv:1712.07158 \[physics.ins-det\]](#).  
[99] Y. Freund and R. E. Schapire, *J. Comput. Syst. Sci.* **55**, 119 (1997).  
[100] A. Hoecker, P. Speckmayer, J. Stelzer, J. Therhaag, E. von Toerne, and H. Voss, *PoS ACAT*, 040 (2007), [arXiv:physics/0703039](#).  
[101] G. Punzi, eConf **C030908**, MODT002 (2003), [arXiv:physics/0308063](#).

## Appendix A: Input variables for multivariate analysis

TABLE VI. MVA input variables for one fat jet event category.

Variable	Rank		Description
	Fixed-radius	Dynamic-radius	
$H_T$	1	1	Scalar $p_T$ sum of jets
$m_{SD}$	2	7	Soft-drop mass of the leading fat jet
$\tau_{21}$	3	6	2-to-1 subjettiness ratio of the leading fat jet
$ \eta_\ell $	4	4	Lepton $ \eta $
$N_{b\text{-jets}}$	5	9	No. of narrow b-jets that are not part of any fat jet
$p_{T,\ell}$	6	3	Lepton $p_T$
$\tau_{32}$	7	10	3-to-2 subjettiness ratio of the leading fat jet
$ \eta_{fj} $	8	5	Leading fat jet $ \eta $
$H_{10}$	9	11	10th order Fox-Wolfram moment
$p_T^{\text{miss}}$	10	10	Missing transverse momentum
$m_T$	11	14	Transverse mass of the lepton- $p_T^{\text{miss}}$ system
$ \eta_j $	12	12	$ \eta $ of the leading narrow jet that is not part of any fat jet
$m_j$	13	15	Mass of the leading narrow jet that is not part of the fat jet
$N_{\text{jets}}$	14	16	Number of narrow jets that are not part of the fat jet
$p_{T,j}$	15	13	$p_T$ of the leading narrow jet that is not part of any fat jet
S	16	17	Sphericity obtained from the eigen values of the momentum tensor [45]
$p_{T,fj}$	17	2	$p_T$ of the leading fat jet
A	18	18	Aplanarity obtained from the eigen values of the momentum tensor [45]

## Appendix B: Cross sections and Branching Ratio Information for Different Mass Points

TABLE VII. Cross sections and branching ratios of various decay modes for different top partner masses. All other parameters are kept the same as in the benchmark point defined in Eq. 7.

$M_T$ [TeV]	$\sigma(pp \rightarrow T\bar{t} + \bar{T}t)$ [fb]	$\Gamma_T$ [GeV]	$\mathcal{B}(T \rightarrow tZ)$	$\mathcal{B}(T \rightarrow th)$	$\mathcal{B}(T \rightarrow tg)$	$\mathcal{B}(T \rightarrow bW)$
1.4	139.81	18.48	41.58%	9.23%	31.68%	17.52%
1.6	78.24	27.67	41.95%	9.09%	31.49%	17.47%
1.8	45.04	39.43	42.24%	9.00%	31.31%	17.45%
2.0	26.51	54.09	42.47%	8.94%	31.13%	17.45%
<b>2.2</b>	<b>15.96</b>	<b>71.96</b>	<b>42.67%</b>	<b>8.90%</b>	<b>30.97%</b>	<b>17.46%</b>
2.4	9.72	93.36	42.84%	8.88%	30.81%	17.47%
2.6	6.04	118.58	42.98%	8.86%	30.67%	17.49%
2.8	3.82	147.94	43.11%	8.85%	30.53%	17.51%
3.0	2.45	181.76	43.22%	8.84%	30.41%	17.53%